The Biophysicist

Designing a Compact, Low-Cost FRET Microscopy Platform for the Undergraduate Classroom

John W. Rupel[1,2,§], Sophia M. Sdao[1,3,§], Kadina E. Johnston[1,2], Ethan T. Nethery[1,2], Kaitlyn A. Gabardi[1,2], Benjamin A. Ratliff[1,2], Zach J. Simmons[2,4], Jack T. Postlewaite[2], Angela M. Kita[3], Jeremy D. Rogers[2,4,*], Matthew J. Merrins[1,3,4,5,*]

[1]Department of Medicine, Division of Endocrinology, Diabetes, and Metabolism, University of Wisconsin–Madison, Madison, WI 53792, USA
[2]Department of Biomedical Engineering, University of Wisconsin–Madison, Madison, WI 53706, USA
[3]Department of Biomolecular Chemistry, University of Wisconsin–Madison, Madison, WI 53706, USA
[4]McPherson Eye Research Institute, University of Wisconsin–Madison, Madison, WI 53705, USA
[5]William S. Middleton Memorial Veterans Hospital, Madison, WI 53705, USA

ABSTRACT Advances in fluorescent biosensors allow researchers to spatiotemporally monitor a diversity of biochemical reactions and secondary messengers. However, commercial microscopes for the specific application of Förster Resonance Energy Transfer (FRET) are prohibitively expensive to implement in the undergraduate classroom, owing primarily to the dynamic range required and need for ratiometric emission imaging. The purpose of this article is to provide a workflow to design a low-cost, FRET-enabled microscope and to equip the reader with sufficient knowledge to compare commercial light sources, optics, and cameras to modify the device for a specific application. We used this approach to construct a microscope that was assembled by undergraduate students with no prior microscopy experience that is suitable for most single-cell cyan and yellow fluorescent protein FRET applications. The utility of this design was demonstrated by measuring small metabolic oscillations by using a lactate FRET sensor expressed in primary mouse pancreatic islets, highlighting the biologically suitable signal-to-noise ratio and dynamic range of our compact microscope. The instructions in this article provide an effective teaching tool for undergraduate educators and students interested in implementing FRET in a cost-effective manner.

KEY WORDS fluorescence; Förster resonance energy transfer; microscopy

I. INTRODUCTION

Fluorescence microscopy is a powerful technique that has revolutionized the field of biology by providing a relatively noninvasive approach to study cellular dynamics. A large selection of fluorescent biosensors is currently available that includes epitope tags for synthetic fluorophores (1–3), dyes (4–6), and genetically encoded sensors (7–9). Förster resonance energy transfer (FRET)–based sensors (10–13) are still the most prevalent and diverse, having been leveraged to measure protein–protein interactions (14–16), small molecules (17–20), enzyme activity (21–24), signal transduction, motility, and other cellular processes (25–28). Despite the accessibility

"§" equal contribution

"*" corresponding authors

Received: 10 August 2019
Accepted: 13 January 2020
Published: 3 June 2020

of nonprofit plasmid repositories for FRET probes (e.g., Addgene) and the widespread agreement that STEM training should begin early (29–33), FRET imaging is not yet widely integrated in undergraduate laboratory curricula, with only a handful of descriptions in educational journals (34–37).

II. SCIENTIFIC AND PEDAGOGIC BACKGROUND

The number of microscopes required for a given classroom scales with the number of students, putting constraints on the cost per instrument. Although several low-cost fluorescence microscope platforms are available, they are designed for more complex applications, such as super-resolution or 3-dimensional imaging (e.g., liteTIRF and OpenSPIM) (38, 39) or are limited by their ability to measure 1 emission wavelength (40–42). FRET imaging in live-cell experiments requires 2 emission wavelengths for donor and acceptor fluorophores to be captured nearly simultaneously, which requires fast emission filter switching or the use of a dichroic mirror and multiple cameras. Considering the limited dynamic range of most FRET sensors, emission signals must be collected at a sufficient signal-to-noise ratio (SNR) to detect small-amplitude modulations in each emission channel. A customized microscope optimized for this application depends on the interplay of all the hardware components. Although hardware manufacturers provide absolute performance specifications (e.g., light source power, objective numeric aperture [NA], and camera read noise), this information is divorced from the performance requirements for any given FRET sensor. Guidelines for matching hardware performance with a specific FRET application would allow for a minimum purchase without overbuying.

This article is intended to provide sufficient guidance for undergraduates and their instructors to optimize and build a FRET microscope from commercial parts. Section IV is organized into 3 major sections (IV.A, IV.B, and IV.C) that describe the design process for tailoring a microscope to suit a particular application, followed by a fourth section (IV.D) that demonstrates the assembled microscope. We also present the photon transfer curve (PTC) method as a valuable tool for empirically assessing a camera to ensure performance requirements for a particular application are met with minimal cost. Finally, we demonstrate the resulting microscope and show that it can detect cytosolic lactate oscillations in primary mouse islets by using the Laconic FRET reporter (43). Thus, we provide a valuable teaching tool in addition to detailed instructions for constructing a customizable, cost-effective FRET microscope.

III. METHODS

A. Mouse islet isolation

All animal studies were approved by the Institutional Animal Care and Use Committees of the University of Wisconsin–Madison and the William S. Middleton Memorial Veterans Hospital. The C57Bl6/J wild-type mice were obtained from the Jackson Laboratory (stock 000664). Islets were isolated as detailed in (44, 45) with modifications (46). Briefly, the mouse pancreas was inflated through the common bile duct by using 3 to 5 mL of 0.67 mg/mL collagenase (C7657, Sigma, St. Louis, MO) and 0.2 mg/mL bovine serum albumin (BSA) in Hanks buffered salt solution (HBSS; Invitrogen, Carlsbad, CA), excised, and incubated in a glass of 5 mL of collagenase, BSA, and HBSS solution for 5 min on orbital shaker at 250 rpm. After 6 min of incubation the digest was agitated for 20 s at 375 rpm every 2 min for an additional 18 min. The pancreatic digest was washed 3 times by pelleting at 50 $\times$ g for 2 min at 4 °C and washing with 30 mL of ice-cold HBSS and BSA solution. Pellets were resuspended in 1 to 2 mL of BSA and HBSS solution by vortexing at medium speed. Islets were handpicked from acinar tissue in 40 mL of ice-cold BSA and HBSS solution.

B. Cloning and adenoviral delivery

The complementary deoxyribonucleic acid for the Laconic FRET biosensor (44238, Addgene, Watertown, MA) was cloned by Gibson

assembly (New England BioLabs, Ipswich, MA) into a modified pENTR-DS shuttle vector (Invitrogen) containing the rat insulin promoter (RIP1) and β-globin intron (BGI) as in a previous study (21). Clonase II was used to prepare the full-length adenovirus in pAD/PL-DEST (Invitrogen), yielding β-cell–specific lactate biosensors (Ad-RIP-BGI-Laconic-pA). Similarly, the D4ER FRET biosensor (47, 48) was synthesized by using gBlocks (IDT, Coralville, IA) to generate adenovirus with β-cell–specific expression of endoplasmic reticulum (ER)–targeted Ca^{2+} biosensors (Ad-RIP-BGI-D4ER-pA). Freshly isolated islets were immediately infected with 1 μL of adenovirus in 2 mL of islet media (RMPI1640 supplemented with 10% fetal bovine serum [v/v], 100 units/mL penicillin, and 100 μg/mL streptomycin; Invitrogen) for 2 h at 37 °C, then moved to fresh media. Experiments were performed 72 h postisolation to allow for sensor expression.

C. Confirmation of sensor expression by 2-photon microscopy

Islets were imaged in no. 1.5 glass-bottom dishes on a multiphoton laser scanning system based around a Nikon TE-300 inverted microscope equipped with a 40×/1.15 NA water immersion objective (Nikon, Tokyo, Japan) in a standard imaging solution (in millimolars: 135 NaCl, 4.8 KCl, 5 $CaCl_2$, 1.2 $MgCl_2$, 10 HEPES, 10 glucose; pH 7.35, and 305 mOsm). Temperature was maintained at 35 °C with a Tokai Hit incubator. The yellow fluorescent protein (YFP) was excited with a Chameleon Ultra laser (Coherent, Santa Clara, CA) at 890 nm. A 535/70 bandpass emission filter (Chroma, Bellows Falls, VT) was used before collection by a Hamamatsu photomultiplier tube. Images were collected at 512 × 512 resolution with a 0.5-μm step size at an optical zoom of 1.5 and dwell time of 2 μs.

D. Widefield ER Ca^{2+} imaging on a research-grade microscope

Islets expressing the D4ER were imaged in an RC-41LP imaging chamber (Warner Instruments, Hamden, CT) on a Nikon Eclipse Ti-E inverted microscope equipped with a Nikon SuperFluor 20×/0.75 NA air objective. The islets were perfused with standard imaging solution (described previously). The flow rate was set to 0.3 mL/min, and the temperature was maintained at 33 °C by using solution and chamber heaters (Warner Instruments). Excitation light was provided by a SOLA SE II 365 (Lumencor, Beaverton, OR) set to 10% output with 2 inline neutral density filters (Nikon ND4 and ND8) that further reduced the excitation intensity by 32-fold. Filters for cyan fluorescent protein (CFP) excitation (ET430/24x), CFP emission (ET470/24m), and YFP emission (ET535/30m) were used in combination with an ET-ECFP/EYFP/mCherry multiband filter set (89006, Chroma) and reported as the YFP:CFP emission ratio (R535/470). Fluorescence emission was collected with a Hamamatsu ORCA-Flash4.0 V2 Digital CMOS camera every 6 s by using 50- to 100-ms exposure times. A single region of interest (ROI) was used to quantify the average response of each islet by using NIS-Elements (Nikon).

IV. RESULTS AND DISCUSSION

To optimize the microscope design, it is important to consider which parameters or hardware components depend on others. Figure 1a shows the flow of decisions used to optimize the design that are discussed in the following sections. Generally, the microscope should be designed around the needs of the application, so we begin by choosing a biosensor. The choice of biosensor determines the spectra involved and therefore the excitation and emission filters, as well as the optimal light source. In addition, the dynamic range of the biosensor places demands on the detection SNR and therefore influences the choice of camera. Note that the camera sensor size and pixel size—while a driving factor in the optimization of commercial microscopes—are a secondary concern because magnification can be modified by the optical design. Next, complementary metal oxide semiconductor (CMOS) cameras are evaluated to compare sensitivity, SNR, and cost. The choice of sample or cell type affects the requirements for field of view (FOV), resolution, and working distance. These parameters determine the optimal ob-

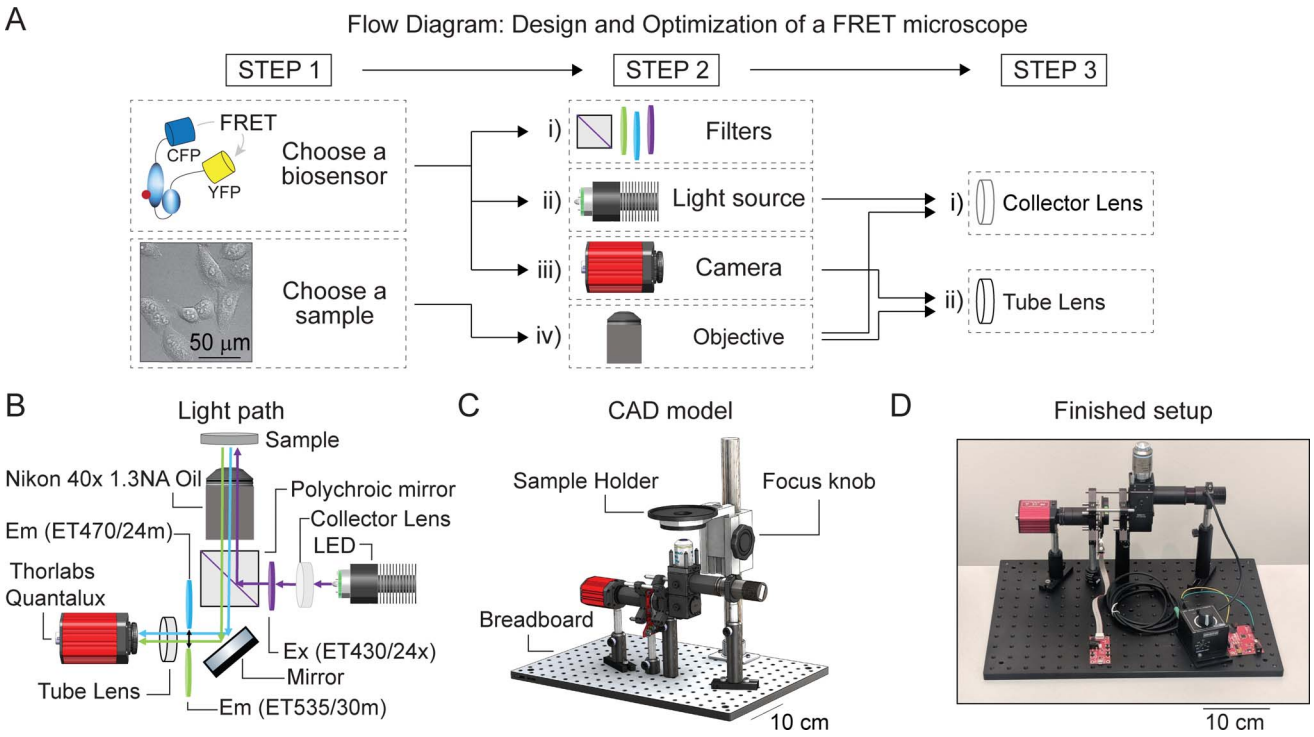

Fig 1. The design of the microscope requires consideration of the choice of biosensor and sample, as well as the optical hardware components. (A) The choice of biosensor informs the choice of filters, light source, and camera, while the sample size informs the choice of microscope objective. The light source and objective inform the optimal collector lens, while the camera and objective inform the optimal tube lens. (B) The light from the LED source is collected by a 35-mm collector lens, passes through a 430/24 nm excitation filter, is reflected off a polychroic mirror, and imaged on the objective pupil to uniformly illuminate the sample. The 470-nm (blue) and 535-nm (green) emission light passes through the polychroic mirror, is reflected off the fold mirror and passes through either a 535/30 nm or a 470/24 nm emission filter. The 50-mm tube lens images the sample onto the camera. (C) The computer-aided design model depicts the final design of the microscope. All components are mounted on posts attached to an optical breadboard, the sample is held by 3-dimensional printed holder, a metal post acts as a support for the rack and pinion focus adjustment, and a square bracket attaches the metal post to the optical breadboard. (D) Photograph of the microscope used to collect data.

jective to use. In the final step, the collector lens is chosen to efficiently couple the light source to the objective, and the tube lens is chosen to couple the objective to the camera with optimal magnification. The resulting design of the assembled microscope is shown in Figures 1b–1d; a list of parts and assembly instructions are provided online in the Supplemental Material. As a demonstration of the assembled microscope, results are presented by using a lactate FRET sensor to observe metabolic oscillations in pancreatic islets.

A. The choice of biosensor governs the choice of filters, light-emitting diode, and camera

FRET efficiency is a sensitive function of the distance between donor and acceptor fluorophores, as well as the relative orientations of the donor emission dipole and the acceptor absorption dipole (13). In the simplest implementation of ratiometric CFP–YFP FRET imaging, a "sandwich" biosensor (49), the donor fluorophore CFP and acceptor fluorophore YFP are covalently linked, and only 2 images are collected. A determination of the FRET efficiency (reported as the percentage of energy transfer) is not required in this case, and FRET is reported as the ratio of YFP acceptor fluorescence at ~535 nm, when the donor is excited with ~430 nm light (DA image: donor excitation, acceptor emission), to the CFP donor fluorescence at ~470 nm, when the donor is excited with ~430 nm light (DD image: donor excitation, donor emission). Note, however, that additional corrections must be made for intermolecular FRET interactions (i.e., when the

donor and acceptor fluorophores are on separate molecules), because FRET efficiency varies with the stoichiometry of donors to acceptors (50, 51). From a hardware perspective, the most important consequence of intermolecular FRET is the need to acquire a third image (AA: acceptor excitation, acceptor emission), which requires an additional light source to directly excite YFP. Because the majority of FRET biosensors are single-chain intramolecular sensors, we focus here on implementing simple ratiometric FRET.

1. Filters

Excitation filter: The excitation and emission filters must match the excitation and emission spectra of the biosensor to maximize efficiency, while minimizing cross talk. That is, to detect FRET, the light source used for excitation of CFP should minimally excite YFP. Figure 2a shows the transmittance of a 430 ± 12 nm excitation filter (ET430/24x, US$325, Spectra Viewer, Chroma Technology Corporation, Bellows Falls, VT, available at https://www.chroma.com/spectra-viewer) superimposed on the fluorescence excitation spectra of CFP and YFP (SearchLight, Semrock, IDEX Health & Science, LLC, West Henrietta, NY, available at https://searchlight.semrock.com), a configuration that ensures sufficient CFP excitation, while minimizing YFP excitation.

Emission filters and polychroic mirror: Among the reasons that a low-cost FRET microscope is more expensive than a low-cost fluorescence microscope is the low quantum yield and photostability of CFP and YFP variants (52–55) relative to brighter, bleach-resistant organic dyes (e.g., cell permeant Janelia Fluor dyes) (56) that can be used in combination with genetically encoded epitope tags (e.g., SNAP-tags or HaloTags, $65 from Addgene) (57–59). There are a number of ways to make up for this deficiency, each involving maximizing the efficiency of light collection. The most cost-effective way to increase light collection efficiency is to use emission filters for CFP and YFP with greater than 95% transmittance, such as the ET470/24m and ET535/30m (Chroma, $325 each), and multiple companies offering CFP–YFP FRET filters will offer a matched

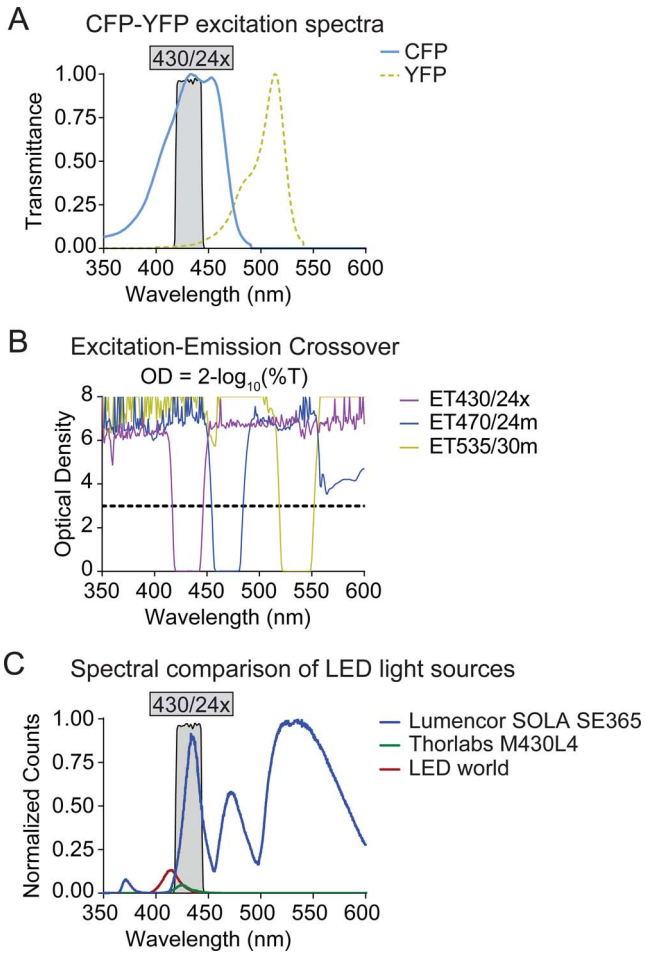

Fig 2. FRET imaging requires illumination spectra that efficiently excites the donor fluorophore, while not exciting the acceptor. (A) For CFP–YFP, a bandpass 430/24x excitation filter maximizes excitation of CFP, while minimizing unwanted excitation of YFP. Fluorophore spectra are exported from the Semrock SearchLight spectra viewer (https://searchlight.semrock.com/). (B) The 430/24x CFP excitation and 470/24m CFP emission filters exhibit an OD greater than or equal to 3 at their crossover point. (C) Comparison of the 3 LED source spectra within the excitation filter. Filter spectra were exported from the Chroma Spectra Viewer (https://www.chroma.com/spectra-viewer).

polychroic mirror for multiple excitation wavelengths (e.g., for intermolecular FRET), even though a long-pass dichroic (e.g., FF458-Di02, $325, Semrock) would otherwise suffice for intramolecular FRET. Any stray light from the light source is much brighter than CFP–YFP and will easily saturate the camera. Thus, an added advantage of using matched filter sets (e.g., 89002, $1,300, Chroma; FRET-CFP/YFP-C, $1,185, Semrock) is they ensure that light passing through the excitation filter is suffi-

ciently blocked by the emission filter. However, any excitation–emission filter pairing will work provided that the CFP excitation filter and CFP emitter exhibit an optical density (OD; i.e., light blocking) greater than or equal to 3 at their crossover point (Fig 2b) (OD spectra are available for each filter are available at https://www.chroma.com/spectra-viewer; Spectra Viewer, Chroma Technology). Note that a wide variety of superior CFP and YFP variants are available (52–55), and guidelines exist for optimizing excitation and detection conditions for the most common variants (60).

2. Light source

The light source is a critical component of FRET microscopy that must deliver sufficient optical power at the appropriate wavelength matched to the chosen excitation filter. Light-emitting diodes (LEDs) are an attractive option because they emit light in a relatively narrow wavelength range, although an excitation filter is still required to improve the specificity of donor excitation. Therefore, the best choice of light source depends on the chosen biosensor, as well as the excitation and emission filters. In addition to these requirements, other considerations include cost, efficiency (minimal light produced outside the excitation band), and ease of mounting to the microscope.

Although narrowband LEDs are more economical, broadband light sources provide more flexibility and are therefore used in commercial microscopes. For example, white-light LEDs (e.g., TLED, 400 to 700 nm, $2,035, Sutter, Novato, CA) and solid state light engines are available that combine multiple LEDs to create broad-spectrum emission from the ultraviolet to near infrared (e.g., SOLA SE 365, 365 to 750 nm, $8,500, Lumencor). We chose the Lumencor SOLA for comparison with 2 lower cost, but less versatile light sources: an unmounted LED (3W UV Purple 420nm, $5, LED World, Calgary, AB, Canada), and a mounted LED (M430L4, $164, Thorlabs, Newton, NJ). An important consideration for using the SOLA SE 365 was reducing the light delivery to avoid photobleaching the YFP-based FRET acceptor (and to a lesser extent, the donor, as CFP variants are more photostable) (52–55). Our research-grade Nikon Ti-E microscope (see section III.C) uses 2 stacked neutral density filters (labeled ND4 and ND8) to attenuate the SOLA light output by 32-fold. The SOLA, when set to 10% output, has a power of 3 mW/nm peak at 430 nm, for a combined attenuation of greater than 99.7%. Significantly lower power (and lower cost) LED sources without ND filters, therefore, have the potential to provide sufficient illumination power.

The spectrum of each light source was assessed by using an Ocean Optics USB 4000 spectrometer (Largo, FL) to collect the illumination delivered to the sample plane without an excitation filter present (Fig 2c). Spectra show that both low-cost LEDs delivered efficient illumination in the CFP band. The unmounted LED was the most affordable option ($5), but also required a separate current source ($20) and machining a custom mount for proper alignment within the microscope. By comparison, the Thorlabs LED ($164) was already mounted and threaded for simple attachment to the microscope, and a matched current source was available (LEDD1B, $305, Thorlabs). The Thorlabs LED, which did not require attenuation in the final design, was chosen as more economical than the SOLA, while providing ease of integration and minimizing the manufacturing required to produce multiple microscopy stations required for an undergraduate laboratory. However, the unmounted LED is a capable alternative when cost outweighs ease of fabrication and assembly.

3. Camera

There are many parameters to consider in choosing a camera for microscopy. Bought off the shelf, the image size and resolution of a commercial microscope are constrained by the fixed tube lens, making pixel size and sensor size important properties to consider. However, by having the flexibility to choose both the objective and tube lens (discussed in the following), the image parameters can be matched to a given image sensor allowing prioritization of other camera parameters, including the SNR, bit depth, and dynamic range. In the next section, we will illustrate the

importance of having chosen a biosensor before the camera, by demonstrating how biosensor measurements can be used to predict the SNR and camera bit-depth required. Subsequently, the photon transfer method is used to assess camera SNR.

4. Predicting required SNR and camera bit depth using the dynamic range of the biosensor

The achievable SNR depends on the bit depth and noise characteristics of a given camera and varies with signal level (counts or digital numbers [DN]). To illustrate the determination of SNR, we used our research-grade microscope with a stereotypic FRET biosensor, D4ER, designed for measuring Ca^{2+} in the ER compartment ($[Ca^{2+}]_{ER}$; Fig 3a) (47, 48). Adenovirus was used to express D4ER selectively in β-cells of intact mouse pancreatic islets by using the insulin promoter. Expression of D4ER was confirmed by 2-photon imaging (Fig 3b). Groups of islets were then imaged by our Nikon widefield microscope in the presence of 10 mM glucose to induce oscillations in $[Ca^{2+}]_{ER}$ (Figs 3c and 3d). Because β-cells within the same islet oscillate in synchrony due to electric coupling by gap junctions (61), the intensity fluctuations in CFP and YFP can be analyzed by using a single ROI drawn around each islet. For successful FRET imaging of $[Ca^{2+}]_{ER}$ oscillations, the camera must have sufficient SNR to detect the smallest signal modulation of each fluorescent channel, which varied by 187 ± 19 and 242 ± 19 DN ($n = 11$) in the DD and DA images, respectively (Fig 3e). The smallest modulation, which occurred in the DD image, was approximately 1.5% of the signal (Fig 3f), setting a minimum acceptable value for camera SNR (100/1.5 = 66). Note that in most cases, this information is available for each biosensor in the seminal publication, where authors will routinely report CFP and YFP intensity changes in addition to the FRET ratio.

5. Using a PTC to assess camera performance

Most scientific camera manufacturers provide specifications, including read noise, dynamic range, and bit depth, but making a direct comparison between cameras is not always

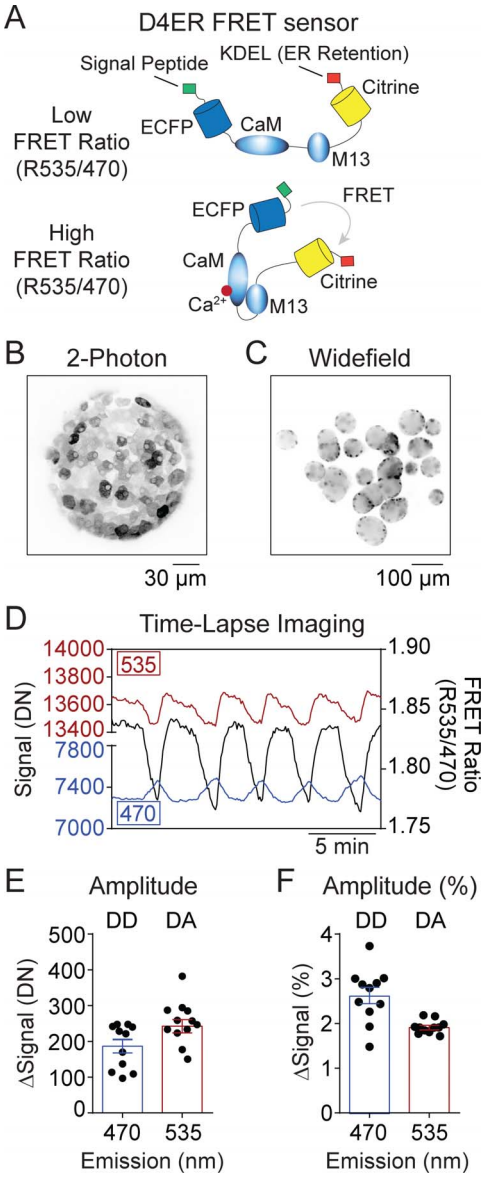

Fig 3. The ER calcium imaging with the FRET sensor D4ER. (A) The D4ER uses an ECFP–citrine FRET pair and an ER-localized calmodulin (CaM) and M13 domain to detect calcium levels in the ER. (Top) In the absence of calcium, the CaM and M13 peptide are dissociated, increasing the distance between the fluorophores and decreasing the citrine:ECFP emission fluorescence ratio. (Bottom) Calcium-binding CaM induces a conformational change allowing M13 to bind, bringing ECFP and citrine closer in space. This increases the FRET efficiency and increases the citrine:ECFP emission fluorescence ratio. (B and C) The D4ER-expressing mouse pancreatic β-cells in intact islets were imaged by using a 2-photon Nikon TE-300 inverted confocal microscope (B) or a widefield Nikon Eclipse Ti-E inverted microscope (C). (D) Representative trace of ER calcium oscillations measured in 10 mM glucose. Intensity changes are shown for the DA (535 emission) and DD images (470 emission), in addition to the FRET ratio (DA:DD). (E and F) The amplitude of ER calcium oscillations ($n = 11$ islets) reported in intensity units (DN) (E) and as a percentage of change (F).

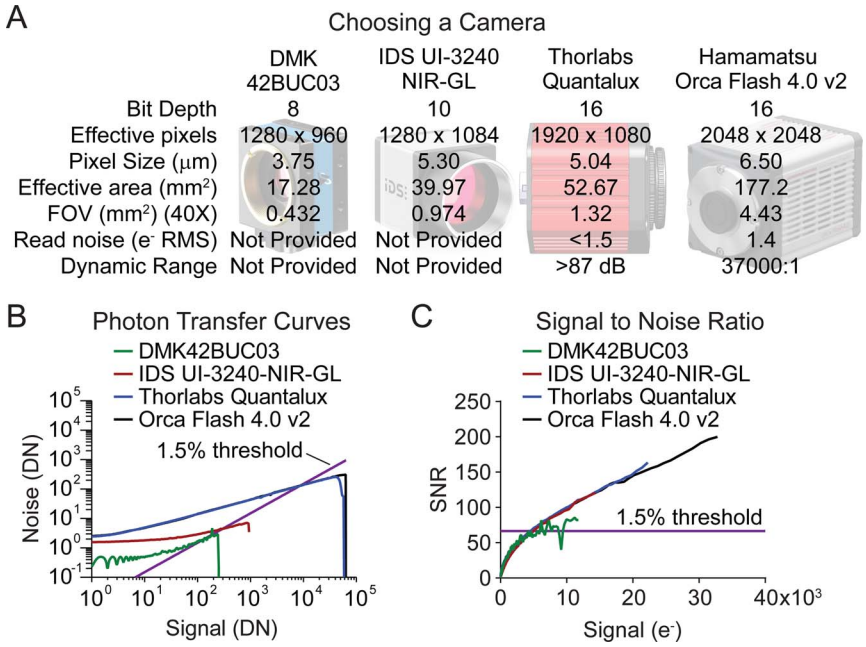

Fig 4. Quantitative determination of camera performance. (A) Camera specifications for each evaluated camera as presented in the specification sheets. (B) A PTC plots noise as a function of signal in terms of DN generated by 4 different cameras, DMK42BUC03, IDS, Quantalux, and ORCA-Flash4.0. A reference line representing a 1.5% change is included; to detect this change in FRET signal, the camera noise must fall below this line. (C) The SNR is plotted as a function of signal in electrons (e^-) for each camera. The reference line (1/1.5% = 66) represents the minimum SNR required; the camera must perform above this line to detect the required 1.5% change in FRET signal.

possible on the basis of these values alone, and lower cost cameras often do not include these values in the documentation. To directly compare camera performance, the PTC method is an excellent tool (62). A PTC is a plot of noise (standard deviation, plotted on the *y* axis) as a function of the average signal (DN, plotted on the *x* axis) detected by the camera, providing a rigorous method for characterizing camera noise for all possible signal values. This only requires a small number of images collected under different signal levels, allowing direct empiric comparison of cameras. The PTC method is, therefore, well suited to evaluating a camera during a demonstration period.

There are 2 main sources of noise to consider: read noise depends on the camera electronics and is independent of signal level, while shot noise increases with the signal detected. Generally, for low signal values, a camera is limited by read noise, while for larger signal values, shot noise is the limiting factor. Read noise is independent of pixel value, so it appears as a constant minimum noise value. Shot noise increases as the square root of the signal, and a PTC is constructed as a log–log plot so that the shot noise manifests as a line with slope of one-half. As a reference, figure 5.1 in (62) illustrates these features. The PTC makes it possible to experimentally confirm and compare camera noise performance that may be difficult to assess using only manufacturer specifications.

Here, we focused on CMOS cameras that have higher speed and resolution (number of pixels), lower noise, and lower cost relative to CCD sensors. We compared 4 CMOS cameras spanning a wide range of cost (in US dollars) and features (Fig 4a). The ORCA-Flash4.0 (Hamamatsu, $16,500) is commonly used for fluorescence imaging and served as a benchmark for camera testing. Three additional lower-cost cameras were evaluated and compared with this benchmark: 8-bit DMK42BUCO3 ($300, The Imaging Source, Charlotte, NC); 10-bit machine vision camera (UI-3240CP-NIR-GL Rev.2: AB00615, $1,600, IDS, Obersulm, Germany, or DCC3240N, Thorlabs); and 16-bit scientific CMOS Quantalux (CS2100M-USB, $3,000, Thorlabs). Of note, we are unaware of

a camera under the $1,000 range that exhibits suitable noise characteristics for FRET.

To generate a PTC, sets of exposures (25 to 100) are acquired with a fixed illumination and exposure time, and the noise is calculated as the standard deviation for each pixel across exposures. To ensure the curve spans the entire range of possible signal values, the procedure is repeated for different integration times or different illumination intensities. Depending on the camera sensor size, a subset of pixels is used to facilitate image collection and processing. We used a 200 × 200 pixel ROI for each camera to generate PTCs. It is also convenient to use nonuniform illumination so that each set of 25 to 100 exposures includes a wide range of pixel values collected simultaneously. Importantly, a set of dark images, when the camera is covered, was acquired for each exposure time used. The average of these dark frames was subtracted to remove dark current and any offset in the analog-to-digital converter (ADC), resulting in a set of background-corrected images. Mean and standard deviation over 25 to 100 frames are then calculated for each pixel, yielding a list of average pixel values and standard deviations. The pixel values are binned, and the noise value for each mean signal bin is calculated by taking the median of the standard deviations in each bin. The median is used in place of the mean as a measure of central tendency because the pixel values are not normally distributed, especially at low values. The median standard deviation of each bin (the noise) is plotted against the average value of each bin (the signal) to generate an experimental PTC (Fig 4b). Example MATLAB scripts for acquiring, processing, and plotting a PTC for a camera are provided along with a small example data set in the GIT repository (https://gitlab.com/rogerslab/edufret; GitLab, San Francisco, CA).

Noise sources added in quadrature with the read noise, a constant, and the shot noise proportional to the average signal. The analog-to-digital sensitivity constant, K_{ADC}, is a measure of how many electrons (e^-) correspond to 1 DN for a given camera. The expression for noise as a function of average signal is shown in Eq. 1, where σ_{total} is the total noise and σ_{read} is the read noise.

$$\sigma_{total} = \sqrt{\sigma_{read}^2 + \frac{\text{average signal}}{K_{ADC}}} \quad (1)$$

Fitting allows determination of K_{ADC} and the read noise from the experimental PTC by using a weighted least squares fit in linear space. Although this application of measuring FRET signal is not read noise limited, being able to fit, extract, and compare read noise is a useful feature of this PTC method and a valuable metric for comparing cameras in applications requiring low signal levels.

The PTC shows the noise as a function of signal. It is also useful to evaluate the SNR, which is calculated for every signal value by dividing the signal by its corresponding standard deviation (Eq. 2), and then plotted as a function of the signal.

$$\text{SNR} = \frac{\text{signal}}{\sigma_{total}} \quad (2)$$

The dynamic range over which sufficient SNR can be achieved is critical in FRET applications. Bit depth can limit dynamic range because one part of 8 bits, a 0.4% change, is a much larger change than one part of 16 bits, a 0.0015% change. CMOS cameras are typically 8 bit (2^8 = 256 DN), 10 bit (2^{10} = 1,024 DN), 12 bit (2^{12} = 4,096 DN), or 16 bit (2^{16} = 65,536 DN). In the absence of noise, the 8-bit camera appears to have sufficient bit depth to detect the 1.5% modulation required for the D4ER FRET biosensor (see subsection IV.A.2 and Fig 3f). However, this is only true when the camera is operating close to saturation. Although the integration time or illumination could be adjusted to ensure the brightest regions of the sample are close to saturation, heterogeneity in the sample results in a range of pixel intensity values. It is typically better to operate with the brightest pixels well below saturation to avoid saturation during the experiment. If a higher signal is delivered to pixels with values already near saturation, data could be lost. The 8-bit camera will, therefore, have a very limited useful range. This illustrates the need to not

only achieve a minimum SNR but to also achieve that SNR over the maximum possible range of pixel values. Because the signal values in counts (DN) are arbitrarily scaled by the camera ADC, cameras with different bit depths can be more easily compared after first converting the signal from DN to e^- by multiplying the average signal value by K_{ADC} (Fig 4c). This also makes it easy to identify the full well capacity as the maximum signal value in e^- for each camera. The usable dynamic range for each camera is the range of values between the minimum SNR threshold for the biosensor and the full well capacity.

To determine whether each camera has sufficient performance, a reference line representing the 1.5% signal change determined in Figure 3f for the D4ER FRET sensor was plotted along with the PTCs of each camera (Fig 4b) and the equivalent reference line (SNR = 66) is shown for the SNR plots (Fig 4c). The camera must perform below the reference line in PTC plots and above the reference line in SNR plots. When part of a camera's PTC is below the reference line, the camera would be able to detect a change of signal less than 1.5% for that range of signal levels. The range of values for which the camera performs better than this reference line is important, so the length of the PTC that was under the reference line was determined in terms of both DN and in terms of e^-, provided this range in DN is convenient for assessing raw values on the camera that are meaningful. This could be used, for example, to set a threshold in which pixel values that have unacceptably poor SNR are removed during analysis. On the other hand, providing this range in e^- allows direct comparison across cameras with different bit depths.

All cameras were able to achieve the required SNR of 66 corresponding to a 1.5% change in signal of the FRET biosensor. However, as discussed previously, the range of signal values over which this SNR is obtained is also important to allow detection across regions of a heterogeneous sample without saturation. The DMK42BUCO3 only achieved SNR of 66 over a range of 6,142 e^- (126 DN), while the IDS UI-3240 and Thorlabs Quantalux exceeded SNR of 66 over range of 9,398 e^- (560 DN) and 17,738 e^- (33,446 DN), respectively. By comparison, the Hamamatsu ORCA-Flash4.0 provided 28,228 e^- (54,109 DN). The ORCA-Flash4.0 provides a number of capabilities not discussed here that may be important in other applications, but for this microscope, the primary requirement was SNR. Because the Quantalux proved comparable to the ORCA-Flash4.0 in this regard at a much lower price, it was chosen for the final design.

Detecting the 2 emission spectral channels can be accomplished by either swapping emission filters and sequentially acquiring frames or dividing the emission spectra with a dichroic beam splitter and using 2 cameras. The latter has the advantage of simultaneous acquisition that may be useful for samples with fast dynamics but has the disadvantage of requiring additional alignment of the images. Although the chosen camera is a cost-effective solution that meets the SNR requirements for FRET, the price for an additional Quantalux camera is still 10× higher than the cost of a motorized filter swapper. Because the acquisition rate possible by using sequential frames after swapping filters was sufficient for this application, a motorized filter slider (ELL6K, $297, Thorlabs) was used.

B. The choice of sample governs the field, resolution, and required working distance, which together determine the optimal objective

FRET biosensors may be used in a variety of cell types ranging from single cells, such as yeast and cell lines, to tissue samples, such as pancreatic islets (Fig 5a). The cell or tissue size affects the required resolution, which for example needs to be higher when looking at small cells, such as yeast, compared with larger mammalian cells. Larger samples, such as pancreatic islets, require a larger FOV to capture an entire islet without stitching. The sample thickness and mounting method may impact the required working distance, defined as the distance between the objective and the focal plane. These considerations, along with

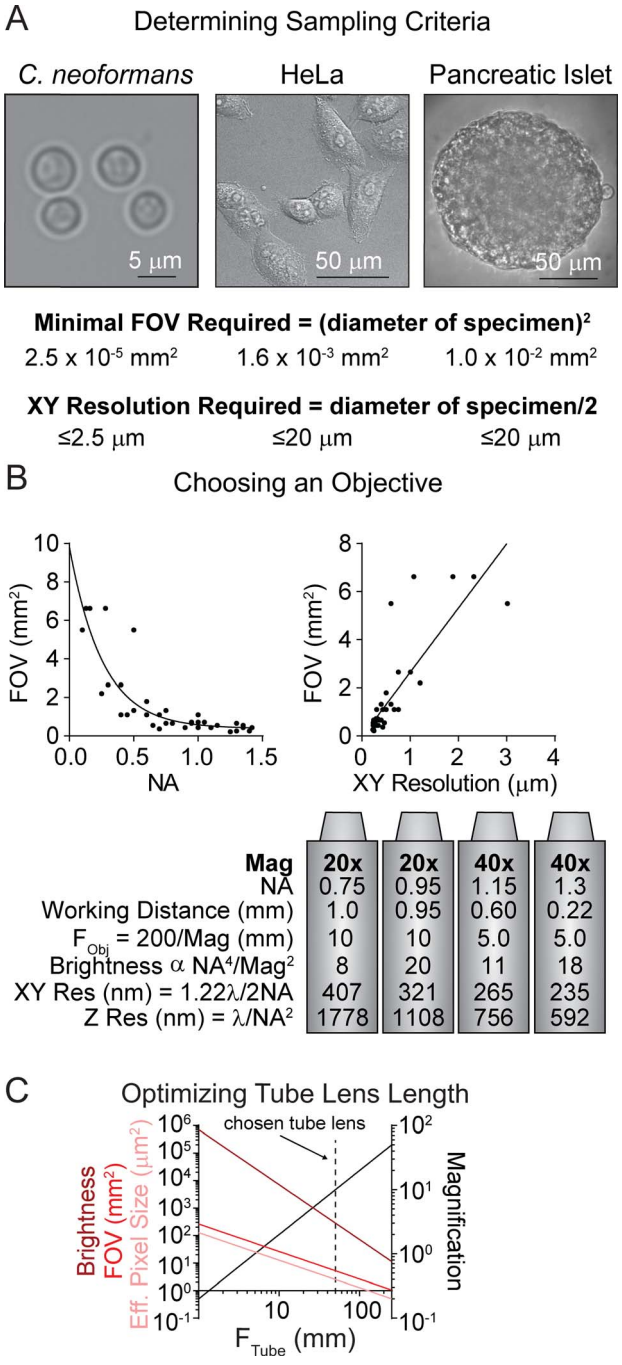

Fig 5. Sample size determines the optimal microscope objective and tube lens length. (A) Minimal FOV and XY resolution required to image yeast cells (*Cryptococcus neoformans*), a human cell line (HeLa) and a mouse pancreatic islet. (B) (Top) The relationship between FOV and NA (right) or XY resolution (left) from 45 commercially available microscope objectives (65). (Bottom) Specifications of commercially available microscope objectives for comparison. (C) Increasing tube lens focal length (F_{Tube}) increases magnification (black line) but decreases brightness, FOV, and effective pixel size.

light collection efficiency, are used to determine the optimal objective.

1. Objective lens

The most important optical element of the microscope is the objective lens. Although higher magnification objectives are associated with higher resolution, maximizing resolution is not always a priority. Note, for example, that when imaging ER calcium in mouse islets, as shown in Figures 3c–3f, it is not necessary to spatially resolve the ER, which is the only source of fluorescent signal due to the ER targeting signal on the FRET sensor itself (47, 48). In this case, the relevant sample was the islet, typically 50 to 300 μm; however, yeasts are an order of magnitude smaller (Fig 5a) and must be individually resolved if their behavior is uncorrelated. High magnification objectives achieve higher resolution by using higher NA, which also collects more of the fluorescence emission. This is critical for maximizing imaging efficiency (minimizing integration time, while reducing phototoxicity). For any given camera and fixed tube lens, the image brightness is improved by the objective NA and diminished by magnification (*m*), which distributes fluorescence emission over more pixels (63).

$$B \propto \frac{NA^4}{m^2} \qquad (3)$$

Higher NA provides better resolution and image brightness, but the increased magnification comes at the cost of reduced FOV, which must accommodate the sample. Figure 5b plots FOV as a function of NA and resolution for a range of objective lenses ranging from 10× to 100× (64). For small samples, such as yeast, high NA and high resolution are prioritized, while for large samples, such as pancreatic islets, the largest NA that still allows sufficient FOV is chosen. Additional specifications are listed for several high NA objectives.

Additional trade-offs of choosing high NA include shorter focal length and therefore small working distance and higher cost. For this application, a 40× oil immersion 1.3 NA (MRF01400, $3,600, Nikon) was selected. The diffraction limited resolution *r* is approximately

0.25 μm for this objective, calculated as

$$r = \frac{1.22\lambda}{2\mathrm{NA}}, \quad (4)$$

where λ is the wavelength (535 nm) being imaged and NA is the numeric aperture of the given objective.

The useable FOV for this objective is approximately 500 μm, and if a 200-mm focal length tube lens were used, the image on the camera would be over 20 mm in diameter, larger than even the largest of the camera sensors. However, the tube lens can be selected as discussed in the following, to provide the desired magnification, FOV, and irradiance on the detector. Note that the choice of camera discussed previously may change the optimal magnification, but this can be modified by selecting another tube lens if a different camera is chosen. The microscope objective is chosen only to maximize light efficiency and provide the desired object plane resolution and FOV for the sample of interest.

C. The choice of light source, camera, and objective governs the choice of collector and tube lenses

1. Collector lens

The illumination optics are chosen to provide efficient, uniform illumination. The LED illumination must be delivered to the sample through the filters and objective. Because the LED intensity is not spatially uniform, imaging the LED onto the sample (critical illumination) would produce a nonuniform illumination and highly variable fluorescent signal. To avoid this, Köhler illumination (65) is used by imaging the LED onto the pupil plane of the objective by using a short focal length collector lens. For a given diameter, a shorter focal length will collect more light from the LED and more efficiently deliver the light to the sample. However, the magnification of the LED image on the back of the objective must also be considered. If the image overfills the objective pupil, light is lost and wasted. On the other hand, if the LED image underfills the objective pupil, the illuminated FOV is reduced. The optical path through the filter cube limits how close the lens can be placed to the objective, so a 35-mm collector (47-634, $95, Edmund Optics, Barrington, NJ) was chosen, and the position was adjusted to produce an image of the LED that just filled the objective pupil.

2. Tube lens

Objectives and tube lenses are designed to be paired. The Nikon 40×/1.3 NA oil objective we chose is designed to be used with a standard (f = 200-mm) tube lens (note this parameter varies by manufacturer and objective). In designing our microscope, we chose the objective on the basis of the sample and NA requirements and chose the camera on the basis of the SNR and dynamic range. We next selected the tube lens to provide the desired magnification of the image onto the camera. A magnification of 40× would also produce a diffraction limit on the detector of $0.25 \times 40 =$ 10 μm, which is larger than the pixel size of all cameras considered. Although oversampling the image resolution can be desirable, resolution was not the primary goal of this work. By choosing a smaller focal length lens to use as a tube lens, the magnification is reduced (while still maintaining the high NA light collection). Figure 5c shows the increase in magnification with tube lens focal length and concurrent decrease in effective pixel size at the object, FOV, and image brightness.

Reducing tube lens focal length from the standard 200 mm reduces magnification and has 3 advantages: increased FOV for a given camera sensor size, closer matching of resolution and pixel size, and increased irradiance on each pixel. The last of these is critical for the application of FRET because, as was shown in the discussion of cameras, the signal needs to be sufficiently high to obtain adequate SNR. To increase signal, or photoelectrons collected in each pixel, there are 3 options, including increasing exposure time, increasing illumination intensity, or decreasing magnification. Exposure time cannot be increased beyond 300 ms, as this makes focusing difficult and adversely affects the data because each fluorescent channel is obtained sequentially. Increasing the illumination intensity is also limited because this begins to cause excess

photobleaching and phototoxicity, limiting the duration that the experiment can be run. Decreasing magnification increases the irradiance by the square of the relative change in magnification (Eq. 3). For this study and the camera chosen previously, the best balance of these constraints was found with a 50-mm tube lens (47-637, Edmund Optics) producing 10× magnification.

D. Demonstration of the assembled microscope: live-cell imaging with a lactate FRET sensor

Previously, we have used fluorescent biosensors in pancreatic islets to measure glucose-stimulated oscillations in metabolites, such as citrate or the ATP:ADP ratio in pancreatic islet β-cells (66, 67). These oscillations are small in magnitude, allowing us to challenge the biologically relevant dynamic range of the microscope. Using our compact microscope, we measured lactate dynamics in live mouse β-cells by using the lactate FRET sensor, Laconic (Fig 6) (43).

Laconic contains a lactate binding domain linked to monomeric teal fluorescent protein (mTFP) and Venus, a YFP (43). The mTFP is the donor fluorophore, and peak excitation occurs at ∼458 nm. The mTFP emits light between 460 and 550 nm, which excites the acceptor fluorophore Venus, which emits light between 500 and 535 nm. When lactate binds Laconic, it induces a conformational change of the Laconic-binding domain, such that the distance between the pair of fluorophores increases. This decreases the FRET transfer efficiency and increases the ratio of mTFP:Venus emission fluorescence (Fig 6a). We expressed Laconic by using the insulin promoter to achieve β-cell expression in live pancreatic islets isolated from mice and imaged lactate dynamics by using the microscope. Note that the excitation filter (430 ± 12 nm) and emission filter (470 ± 12 nm) of our microscope are designed for CFP, which does not precisely match the excitation and emission spectra of mTFP (68, 69), while the spectra of YFP and Venus are closely matched.

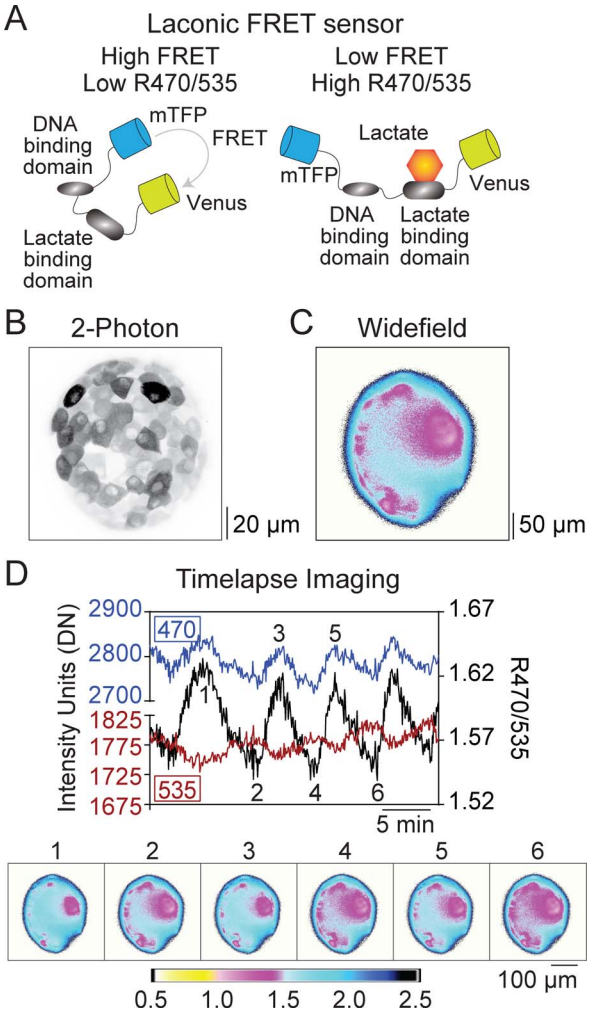

Fig 6. Lactate dynamics in live mouse β-cells in intact islets. (A) A schematic of how lactate binding to the Laconic sensor demonstrates how measured changes in FRET reflect changes in lactate levels. (B and C) Laconic-expressing mouse pancreatic β-cells in intact islets were imaged by using a 2-photon microscope (B) or our custom microscope (C). (D) Lactate levels were measured over 30 min in 10 mM glucose. Colorized images of the islet correspond to the peaks (1,3,5) and troughs (2,4,6) of the FRET ratio (black).

Islets infected with the Laconic biosensor were first subjected to 2-photon imaging to confirm sensor expression (Fig 6b). The islets were then placed in a no. 1.5 glass-bottom dish containing 2 mL of imaging media, and the dish was transferred to a heated platform (33 °C), resting on the sample holder of the compact microscope, and widefield images were captured (Fig 6c). The mTFP was excited by using the Thorlabs M430L4 LED with the intensity knob set to 2/6. The DD and DA images were sequentially captured every 4 s by

using ET470/24m and ET535/30m emission filters, respectively. The camera exposure time was 300 ms for mTFP and 50 ms for Venus. In the presence of a stimulatory glucose concentration (10 mM), we observed slow oscillations in the mTFP and Venus channels, resulting in ratiometric oscillations in the mTFP:Venus FRET ratio (Fig 6d). This validates the ability of the microscope to detect small changes in fluorescence and provides evidence of lactate oscillations in pancreatic β-cells.

V. CONCLUSIONS

We provide the workflow to design a custom, low-cost educational microscope and provide a specific example design to measure FRET dynamics in living cells. We describe methods to provide evidence-based justification on each component choice and identify cost-effective alternatives to expensive parts. We engineered an adenovirus expressing the FRET sensor Laconic under control of the β-cell–specific insulin promoter to generate a novel tool for islet biologists to measure lactate dynamics in live cells. Excitingly, we used our own microscope to measure slow oscillations in cytosolic lactate levels in pancreatic β-cells. Additional experiments will be necessary to determine the significance of lactate oscillations in pancreatic β-cells. The MATLAB scripts for acquiring images use the MicroManager library via MMCore (70). Future work includes the refinement of a custom MATLAB graphical user interfaces for easy data collection, processing, and analysis, as well as code for acquisition and generation of PTCs, which are in continued development and available at GitLab: http://gitlab.com/rogerslab/edufret.

SUPPLEMENTAL MATERIAL

Supplemental material for this article is available at: https://doi.org/10.35459/tbp.2019.000117.S1 and https://doi.org/10.35459/tbp.2019.000117.S2.

ACKNOWLEDGMENTS

The authors thank University of Wisconsin–Madison colleagues Sébastien Ortiz and Christina Hull for providing an image of *Cryptococcus neoformans* and Steve Trier and Melissa Skala for supporting the 2-photon microscope. This research was supported by an Education Innovation Small Grant from the University of Wisconsin–Madison (to MJM and AMK), as well as separate awards to JDR (Retina Research Foundation, Edwin and Dorothy Gamewell Professor, and National Science Foundation CAREER 1845801) and MJM (R01DK113103 and R01AG062328). This work was supported by using facilities and resources from the William S. Middleton Memorial Veterans Hospital. This work does not represent the views of the Department of Veterans Affairs or the US government.

AUTHOR CONTRIBUTIONS

MJM conceived the project. JRR, SMS, KEJ, ETN, KAG, BAR, ZJS, and JTP performed experiments. MJM, JDR, and AMK secured funding. JWR, SMS, JDR, and MJM wrote the manuscript, and all authors edited and approved the manuscript.

REFERENCES

1. Crivat, G., and J. W. Taraska. 2012. Imaging proteins inside cells with fluorescent tags. *Trends Biotechnol* 30:8–16.
2. Li, C., A. G. Tebo, and A. Gautier. 2017. Fluorogenic labeling strategies for biological imaging. *Int J Mol Sci* 18(7):E1473.
3. Freidel, C., S. Kaloyanova, and K. Peneva. 2016. Chemical tags for site-specific fluorescent labeling of biomolecules. *Amino Acids* 48:1357–1372.
4. Lavis, L. D. 2017. Teaching old dyes new tricks: biological probes built from fluoresceins and rhodamines. *Annu Rev Biochem* 86:825–843.
5. Hawe, A., M. Sutter, and W. Jiskoot. 2008. Extrinsic fluorescent dyes as tools for protein characterization. *Pharm Res* 25:1487–1499.
6. Terai, T., and T. Nagano. 2013. Small-molecule fluorophores and fluorescent probes for bioimaging. *Pflugers Arch* 465:347–359.
7. Bolbat, A., and C. Schultz. 2017. Recent developments of genetically encoded optical sensors for cell biology. *Biol Cell* 109:1–23.
8. Specht, E. A., E. Braselmann, and A. E. Palmer. 2017. A critical and comparative review of fluorescent tools for live-cell imaging. *Annu Rev Physiol* 79:93–117.
9. Sanford, L., and A. Palmer. 2017. Recent advances in development of genetically encoded fluorescent sensors. *Methods Enzymol* 589:1–49.
10. Hochreiter, B., A. P. Garcia, and J. A. Schmid. 2015. Fluorescent proteins as genetically encoded FRET biosensors in life sciences. *Sensors (Basel)* 15:26281–26314.
11. Lindenburg, L., and M. Merkx. 2014. Engineering genetically encoded FRET sensors. *Sensors (Basel)* 14:11691–11713.
12. Zadran, S., S. Standley, K. Wong, E. Otiniano, A. Amighi, and M. Baudry. 2012. Fluorescence resonance energy transfer (FRET)-based biosensors: visualizing cellular dynamics and bioenergetics. *Appl Microbiol Biotechnol* 96:895–902.
13. Algar, W. R., N. Hildebrandt, S. S. Vogel, and I. L. Medintz. 2019. FRET as a biomolecular research tool—understanding its potential while avoiding pitfalls. *Nat Methods* 16:815–829.
14. Song, Y., V. G. J. Rodgers, J. S. Schultz, and J. Liao. 2012. Protein interaction affinity determination by quantitative FRET technology. *Biotechnol Bioeng* 109:2875–2883.
15. Margineanu, A., J. J. Chan, D. J. Kelly, S. C. Warren, D. Flatters, S. Kumar, M. Katan, C. W. Dunsby, and P. M. W. French. 2016. Screening for protein-protein interactions using Förster resonance energy transfer (FRET) and fluorescence lifetime imaging microscopy (FLIM). *Sci Rep* 6:28186.
16. Rainey, K. H., and G. H. Patterson. 2019. Photoswitching FRET to monitor protein-protein interactions. *Proc Natl Acad Sci U S A* 116:864–873.
17. Sekar, R. B., and A. Periasamy. 2003. Fluorescence resonance energy transfer (FRET) microscopy imaging of live cell protein localizations. *J Cell Biol* 160:629–633.
18. David Gerecht, P. S., M. A. Taylor, and J. D. Port. 2010. Intracellular localization and interaction of mRNA binding proteins as detected by FRET. *BMC Cell Biol* 11:69.

19. Chen, Y., J. D. Mills, and A. Periasamy. 2003. Protein localization in living cells and tissues using FRET and FLIM. *Differentiation* 71:528–541.
20. Leavesley, S. J., A. Nakhmani, Y. Gao, and T. C. Rich. 2015. Automated image analysis of FRET signals for subcellular cAMP quantification. *Methods Mol Biol* 1294:59–70.
21. Merrins, M. J., A. R. Van Dyke, A. K. Mapp, M. A. Rizzo, and L. S. Satin. 2013. Direct measurements of oscillatory glycolysis in pancreatic islet β-cells using novel fluorescence resonance energy transfer (FRET) biosensors for pyruvate kinase M2 activity. *J Biol Chem* 288:33312–33322.
22. Blum, Y., R. D. Fritz, H. Ryu, and O. Pertz. 2017. Measuring ERK activity dynamics in single living cells using FRET biosensors. *Methods Mol Biol* 1487:203–221.
23. Zhou, X., K. J. Herbst-Robinson, and J. Zhang. 2012. Visualizing dynamic activities of signaling enzymes using genetically encodable FRET-based biosensors from designs to applications. *Methods Enzymol* 504:317–340.
24. Colombo, S., S. Broggi, M. Collini, L. D'Alfonso, G. Chirico, and E. Martegani. 2017. Detection of cAMP and of PKA activity in *Saccharomyces cerevisiae* single cells using fluorescence resonance energy transfer (FRET) probes. *Biochem Biophys Res Commun* 487:594–599.
25. Giepmans, B. N. G., S. R. Adams, M. H. Ellisman, and R. Y. Tsien. 2006. The fluorescent toolbox for assessing protein location and function. *Science* 312:217–224.
26. San Martín, A., S. Ceballo, F. Baeza-Lehnert, R. Lerchundi, R. Valdebenito, Y. Contreras-Baeza, K. Alegría, and L. F. Barros. 2014. Imaging mitochondrial flux in single cells with a FRET sensor for pyruvate. *PLOS ONE* 9:e85780.
27. Elliott, A. D., N. Bedard, A. Ustione, M. A. Baird, M. W. Davidson, T. Tkaczyk, and D. W. Piston. 2017. Hyperspectral imaging for simultaneous measurements of two FRET biosensors in pancreatic β-cells. *PLOS ONE* 12:e0188789.
28. Greotti, E., A. Wong, T. Pozzan, D. Pendin, and P. Pizzo. 2016. Characterization of the ER-targeted low affinity Ca^{2+} probe D4ER. *Sensors (Basel)* 16(9):E1419.
29. Gregerman, S. R., J. S. Lerner, W. von Hippel, J. Jonides, and B. A. Nagda. 1998. Undergraduate student-faculty research partnerships affect student retention. *Rev High Educ* 22:55–72.
30. Campbell, A., and G. Skoog. 2004. Preparing undergraduate women for science careers: facilitating success in professional research. *J Coll Sci Teach* 33:24–26.
31. Summers, M. F., and F. A. Hrabowski. 2006. Preparing minority scientists and engineers. *Science* 311:1870–1871.
32. Lopatto, D. 2007. Undergraduate research experiences support science career decisions and active learning. *CBE Life Sci Educ* 6:297–306.
33. Russell, S. H., M. P. Hancock, and J. McCullough. 2007. Benefits of undergraduate research experiences. *Science* 316:548–549.
34. Jones, J., R. Heim, E. Hare, J. Stack, and B. A. Pollok. 2000. Development and application of a GFP-FRET intracellular caspase assay for drug screening. *J Biomol Screen* 5:307–317.
35. Kugel, J. F. 2008. Using FRET to measure the angle at which a protein bends DNA. *Biochem Mol Biol Educ* 36:341–346.
36. Witherow, D. S., and S. Carson. 2011. A laboratory-intensive course on the experimental study of protein–protein interactions. *Biochem Mol Biol Educ* 39:300–308.
37. Pazhani, Y., A. E. Horn, L. Grado, and J. F. Kugel. 2016. Evaluating the relationship between FRET changes and distance changes using DNA length and restriction enzyme specificity. *J Chem Educ* 93:383–386.
38. Auer, A., T. Schlichthaerle, J. B. Woehrstein, F. Schueder, M. T. Strauss, H. Grabmayr, and R. Jungmann. 2018. Nanometer-scale multiplexed super-resolution imaging with an economic 3D-DNA-PAINT microscope. *ChemPhysChem* 19:3024–3034.
39. Pitrone, P. G., J. Schindelin, L. Stuyvenberg, S. Preibisch, M. Weber, K. W. Eliceiri, J. Huisken, and P. Tomancak. 2013. OpenSPIM: an open-access light-sheet microscopy platform. *Nat Methods* 10:598–599.
40. Miller, A. R., G. L. Davis, Z. M. Oden, M. R. Razavi, A. Fateh, M. Ghazanfari, F. Abdolrahimi, S. Poorazar, F. Sakhaie, R. J. Olsen, A. R. Bahrmand, M. C. Pierce, E. A. Graviss, and R. Richards-Kortum. 2010. Portable, battery-operated, low-cost, bright field and fluorescence microscope. *PLOS ONE* 5:e11890.
41. Zhang, Y. S., J. Ribas, A. Nadhman, J. Aleman, Š. Selimović, S. C. Lesher-Perez, T. Wang, V. Manoharan, S.-R. Shin, A. Damilano, N. Annabi, M. R. Dokmeci, S. Takayama, and A. Khademhosseini. 2015. A cost-effective fluorescence mini-microscope for biomedical applications. *Lab Chip* 15:3661–3669.
42. Hasan, M. M., M. W. Alam, K. A. Wahid, S. Miah, and K. E. Lukong. 2016. A low-cost digital microscope with real-time fluorescent imaging capability. *PLOS ONE* 11:e0167863.
43. San Martín, A., S. Ceballo, I. Ruminot, R. Lerchundi, W. B. Frommer, and L. F. Barros. 2013. A genetically encoded FRET lactate sensor and its use to detect the Warburg effect in single cancer cells. *PLOS ONE* 8:e57712.
44. Neuman, J. C., N. A. Truchan, J. W. Joseph, and M. E. Kimple. 2014. A method for mouse pancreatic islet isolation and intracellular cAMP determination. *J Vis Exp* 2014(88):50374.
45. Villarreal, D., G. Pradhan, C.-S. Wu, C. D. Allred, S. Guo, and Y. Sun. 2019. A simple high efficiency protocol for pancreatic islet isolation from mice. *J Vis Exp* 2019(15):57048.
46. De Leon, E. R., J. A. Brinkman, R. J. Fenske, T. Gregg, B. A. Schmidt, D. S. Sherman, N. E. Cummings, D. C. Peter, M. E. Kimple, D. W. Lamming, and M. J. Merrins. 2018. Age-dependent protection of insulin secretion in diet induced obese mice. *Sci Rep* 8:17814.
47. Ravier, M. A., D. Daro, L. P. Roma, J.-C. Jonas, R. Cheng-Xue, F. C. Schuit, and P. Gilon. 2011. Mechanisms of control of the free Ca^{2+} concentration in the endoplasmic reticulum of mouse pancreatic β-cells: interplay with cell metabolism and $[Ca^{2+}]c$ and role of SERCA2b and SERCA3. *Diabetes* 60:2533–2545.
48. Johnson, J. S., T. Kono, X. Tong, W. R. Yamamoto, A. Zarain-Herzberg, M. J. Merrins, L. S. Satin, P. Gilon, and C. Evans-Molina. 2014. Pancreatic and duodenal homeobox protein 1 (Pdx-1) maintains endoplasmic reticulum calcium levels through transcriptional regulation of sarco-endoplasmic reticulum calcium ATPase 2b (SERCA2b) in the islet β cell. *J Biol Chem* 289:32798–32810.
49. Shimozono, S., and A. Miyawaki. 2008. Engineering FRET constructs using CFP and YFP. *Methods Cell Biol* 85:381–393.
50. Hoppe, A., K. Christensen, and J. A. Swanson. 2002. Fluorescence resonance energy transfer-based stoichiometry in living cells. *Biophys J* 83:3652–3664.
51. D'Andrea-Merrins, M., L. Chang, A. D. Lam, S. A. Ernst, and E. L. Stuenkel. 2007. Munc18c interaction with syntaxin 4 monomers and SNARE complex intermediates in GLUT4 vesicle trafficking. *J Biol Chem* 282:16553–16566.
52. Shaner, N. C., P. A. Steinbach, and R. Y. Tsien. 2005. A guide to choosing fluorescent proteins. *Nat Methods* 2:905–909.
53. Day, R. N., and M. W. Davidson. 2012. Fluorescent proteins for FRET microscopy: monitoring protein interactions in living cells. *BioEssays* 34:341–350.
54. Bajar, B. T., E. S. Wang, S. Zhang, M. Z. Lin, and J. Chu. 2016. A guide to fluorescent protein FRET pairs. *Sensors (Basel)* 16(9):1488.
55. Rodriguez, E. A., R. E. Campbell, J. Y. Lin, M. Z. Lin, A. Miyawaki, A. E. Palmer, X. Shu, J. Zhang, and R. Y. Tsien. 2017. The growing and glowing toolbox of fluorescent and photoactive proteins. *Trends Biochem Sci* 42:111–129.
56. Grimm, J. B., A. K. Muthusamy, Y. Liang, T. A. Brown, W. C. Lemon, R. Patel, R. Lu, J. J. Macklin, P. J. Keller, N. Ji, and L. D. Lavis. 2017. A general method to fine-tune fluorophores for live-cell and in vivo imaging. *Nat Methods* 14:987–994.
57. Keppler, A., S. Gendreizig, T. Gronemeyer, H. Pick, H. Vogel, and K. Johnsson. 2003. A general method for the covalent labeling of fusion proteins with small molecules *in vivo*. *Nat Biotechnol* 21:86–89.
58. Los, G. V., L. P. Encell, M. G. McDougall, D. D. Hartzell, N. Karassina, C. Zimprich, M. G. Wood, R. Learish, R. F. Ohana, M. Urh, D. Simpson, J. Mendez, K. Zimmerman, P. Otto, G. Vidugiris, J. Zhu, A. Darzins, D. H. Klaubert, R. F. Bulleit, and K. V. Wood. 2008. HaloTag: a novel protein labeling technology for cell imaging and protein analysis. *ACS Chem Biol* 3:373–382.
59. Erdmann, R. S., S. W. Baguley, J. H. Richens, R. F. Wissner, Z. Xi, E. S. Allgeyer, S. Zhong, A. D. Thompson, N. Lowe, R. Butler, J. Bewersdorf, J. E. Rothman, D. St Johnston, A. Schepartz, and D. Toomre. 2019. Labeling strategies matter for super-resolution microscopy: a comparison between HaloTags and SNAP-tags. *Cell Chem Biol* 26:584–592.e6.
60. Rizzo, M. A., G. Springer, K. Segawa, W. R. Zipfel, and D. W. Piston. 2006. Optimization of pairings and detection conditions for measurement of FRET between cyan and yellow fluorescent proteins. *Microsc Microanal* 12:238–254.
61. Benninger, R. K. P., M. Zhang, W. S. Head, L. S. Satin, and D. W. Piston. 2008. Gap junction coupling and calcium waves in the pancreatic islet. *Biophys J* 95:5048–5061.
62. Janesick, J., K. Klaasen, and T. Elliott. 1987. Charge-coupled-device charge-collection efficiency and the photon-transfer technique. *Opt Eng* 26(10):261072.
63. Herman, B. 2002. Fluorescence microscopy. *Curr Protoc Immunol* 48(1):21.2.1–21.2.10.
64. Bumstead, J. R., J. J. Park, I. A. Rosen, A. W. Kraft, P. W. Wright, M. D. Reisman, D. C. Côté, and J. P. Culver. 2018. Designing a large field-of-view two-photon microscope using optical invariant analysis. *Neurophotonics* 5:025001.

65. Evennett, P. 1983. Kohler illumination: a simple interpretation. *Proc Royal Microsc Soc* 28(4):189–192.
66. Gregg, T., C. Poudel, B. A. Schmidt, R. S. Dhillon, S. M. Sdao, N. A. Truchan, E. L. Baar, L. A. Fernandez, J. M. Denu, K. W. Eliceiri, J. D. Rogers, M. E. Kimple, D. W. Lamming, and M. J. Merrins. 2016. Pancreatic β-cells from mice offset age-associated mitochondrial deficiency with reduced K_{ATP} channel activity. *Diabetes* 65:2700–2710.
67. Gregg, T., S. M. Sdao, R. S. Dhillon, J. W. Rensvold, S. L. Lewandowski, D. J. Pagliarini, J. M. Denu, and M. J. Merrins. 2019. Obesity-dependent CDK1 signaling stimulates mitochondrial respiration at complex I in pancreatic β-cells. *J Biol Chem* 294(12):4656–4666.
68. Ai, H., J. N. Henderson, S. J. Remington, and R. E. Campbell. 2006. Directed evolution of a monomeric, bright and photostable version of *Clavularia* cyan fluorescent protein: structural characterization and applications in fluorescence imaging. *Biochem J* 400:531–540.
69. Day, R. N., C. F. Booker, and A. Periasamy. 2008. Characterization of an improved donor fluorescent protein for Förster resonance energy transfer microscopy. *J Biomed Opt* 13:031203.
70. Edelstein, A. D., M. A. Tsuchida, N. Amodaj, H. Pinkard, R. D. Vale, and N. Stuurman. 2014. Advanced methods of microscope control using μManager software. *J Biol Methods* 1(2):e10.